

# 15

## High-precision laser stabilization via optical cavities

MICHAEL J. MARTIN AND JUN YE

### 15.1 Introduction

Optical cavities are extremely useful devices in laser-based research. Within the context of precision measurement, they enable tests of the laws that govern the macroscopic structure of the universe, embodied in the search for gravitational waves (Abbott and The LIGO Scientific Collaboration, 2009) (see also Chapter 14). At the other end of the length scale, cavity-stabilized lasers are powerful tools for precision spectroscopy that probe nature at the quantum mechanical level, through tests of quantum electrodynamics (QED) (Kolachevsky *et al.*, 2009). Furthermore, cavities enable high-sensitivity broadband spectroscopy (Thorpe *et al.*, 2006), which has practical applications in trace gas sensing; exploration of new light-matter interaction regimes in cavity QED (Miller *et al.*, 2005) (see also Chapter 17); tests of fundamental physical principles including relativity (Brillet and Hall, 1979; Hils and Hall, 1990; Eisele *et al.*, 2009), local position invariance (Blatt *et al.*, 2008), and the time invariance of the fundamental constants of nature (Fortier *et al.*, 2007b); and nonlinear optics, including coherent light build-up for studies of extremely nonlinear effects (Gohle *et al.*, 2005; Yost *et al.*, 2009). In general, optical cavities have become indispensable tools at the heart of many modern experiments.

In conjunction with optical frequency combs, cavity-stabilized laser systems have enabled the development of highly accurate frequency standards based on neutral atoms (Sterr *et al.*, 2004; Takamoto *et al.*, 2005; Ludlow *et al.*, 2006; Le Targat *et al.*, 2006; Ludlow *et al.*, 2008; Lemke *et al.*, 2009) and trapped ions (Diddams *et al.*, 2001; Madej *et al.*, 2004; Margolis *et al.*, 2004; Rosenband *et al.*, 2008). In recent years, two ion-based standards (Oskay *et al.*, 2006; Chou *et al.*, 2010), and also a neutral atom-based standard (Ludlow *et al.*, 2008) have surpassed the fractional frequency uncertainty of the primary cesium frequency standards that define the SI second (Heavner *et al.*, 2005; Bize *et al.*, 2005).

In addition to better accuracy, the real power of optical frequency standards is precision and stability (Hollberg *et al.*, 2005b). Ultrastable lasers paired with ultranarrow atomic

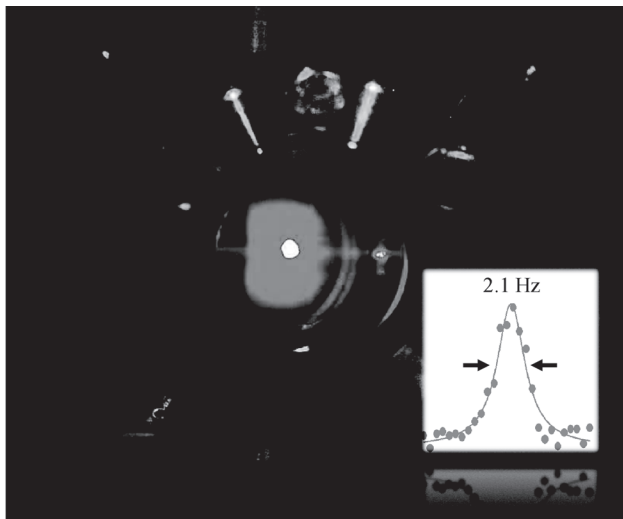


Figure 15.1 Strontium atoms trapped in a magneto-optical trap at JILA. Florescence from laser cooling at 461 nm, the first stage in a cooling process that creates optical lattice-trapped samples at  $\mu\text{K}$  temperatures, is visible from the atomic cloud (center). This same florescence serves as the clock readout. Inset: precision spectroscopy of the ultranarrow  $^1\text{S}_0 \rightarrow ^3\text{P}_0$  clock transition in  $^{87}\text{Sr}$  at 429 THz. This is one of the highest Q spectroscopic features ever observed (Ludlow *et al.*, 2007). (Figure from Zelevinsky *et al.* (2008), Copyright Wiley-VCH Verlag GmbH & Co. KGaA. Reproduced with permission.)

transitions in the optical domain (Figure 15.1) have allowed the realization of optical clocks that are orders of magnitude more stable than current microwave-based frequency references. With increased stability, highly precise measurements of intricate physical effects can be made in short periods of time. For example, collisional effects between ultracold atoms that cause frequency shifts at the  $10^{-16}$  level can be resolved within a few hours time (Campbell *et al.*, 2009). This measurement precision is only possible because the lasers at the heart of the best optical atomic clocks now operate at or below the  $1 \times 10^{-15}$  fractional frequency instability level with a mere 1 s averaging time.

The desire to further improve the stability of optical clocks continues to drive advances in cavity-stabilized laser systems. However, the cavity mirror coating and substrate thermal noise limits the stability of these optical systems in a fundamental way. Presently, this noise is a limiting factor in some of the best optical standards.

## 15.2 Review of optical cavities

A basic optical cavity is formed by an array of two opposite-facing mirrors (Figure 15.2). For high-precision frequency stabilization, these mirrors are typically held apart by a rigid spacer and are kept under vacuum to eliminate a varying intra-cavity index of refraction due to air. Although more complicated cavity geometries exist, including ring-type cavities

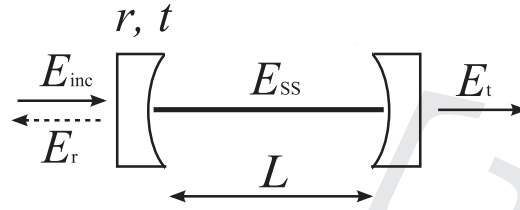


Figure 15.2 Schematic of an optical cavity in the standing wave configuration. The mirror amplitude reflectivity and transmission coefficients are given by  $r$  and  $t$ , respectively.  $E_{SS}$  is the steady-state electric field for a given incident field,  $E_{inc}$ . Some of  $E_{inc}$  is transmitted as  $E_t$ , while some is reflected as  $E_r$ .

(e.g. a cavity formed from a triangular mirror configuration) where the optical field is a running wave, we consider only this basic configuration as it is most common for precision frequency stabilization. For an incident laser of electric field amplitude  $E_{inc}$ , the steady-state electric field inside such a cavity,  $E_{SS}$ , is obtained by enforcing the condition

$$E_{SS} = E_{SS}e^{i\varphi}r^2 + E_{inc}t. \quad (15.1)$$

Here,  $\varphi$  is the round-trip phase accumulated by the light,  $t$  is the mirror field amplitude transmission coefficient and  $r$  is the corresponding amplitude reflectivity. In the absence of mirror absorption and scatter, it is possible to relate the magnitude of the  $r$  and  $t$  coefficients by  $|r|^2 + |t|^2 = 1$ , however we choose to allow for the real-world situation, where mirror losses are influential, by leaving these distinct. The cavity phase shift,  $\varphi$ , can be re-written in terms of the cavity length,  $L$ , and the laser's optical frequency,  $\omega = 2\pi\nu$ , as

$$\varphi = \frac{2L\omega}{c} + \tilde{\varphi}. \quad (15.2)$$

The term  $\tilde{\varphi}$  is due to an additional mode-dependent diffraction phase term. While its consideration is necessary for finding the longitudinal mode-dependent frequency structure of an optical cavity, we omit this term for the remainder of this chapter because we will consider only a single optical mode. We also note that the cavity length,  $L$ , includes the effects of optical field penetration into the mirror coating, which typically requires a correction to the physical length on the order of an optical wavelength. For macroscopic cavities, this effect is negligible, but it becomes important for cavities whose size is of the order of an optical wavelength (Hood *et al.*, 2001).

By solving Equation 15.1 for the steady-state field, we find that the transmitted field amplitude, given by  $E_t = tE_{SS}$ , is

$$\frac{E_t(\nu)}{E_{inc}(\nu)} = \frac{e^{i\varphi/2}t^2}{1 - e^{i\varphi}r^2}. \quad (15.3)$$

Similarly, the reflected field,  $E_r$ , is given by

$$\frac{E_r(\nu)}{E_{inc}(\nu)} \equiv \mathcal{R} = r \left[ \frac{1 - e^{i\varphi}(r^2 + t^2)}{1 - e^{i\varphi}r^2} \right]. \quad (15.4)$$

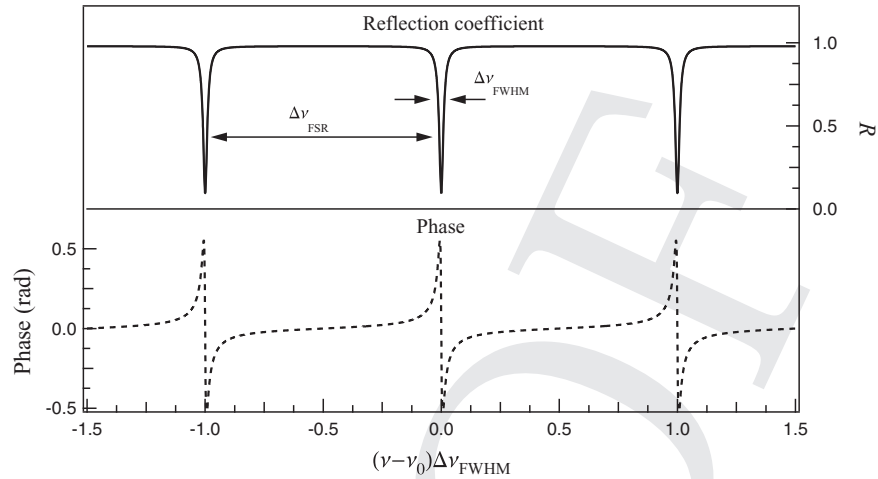


Figure 15.3 Reflection coefficient and corresponding phase shift of the reflected light incident upon an optical cavity. If there are no mirror losses, there is a discontinuity in phase as the reflected light drops to zero. Here, a small mirror loss term has been included, causing the reflection dip to not reach zero.

The cavity reflection transfer function,  $\mathcal{R}$ , is plotted in Figure 15.3. As can be seen from Equations 15.3 and 15.4, the transmission (reflection) is maximized (minimized) when the round trip phase is a multiple of  $2\pi$ . When this condition is met, the cavity is said to be on resonance. This results in the resonance condition

$$\nu_n = n \frac{c}{2L}, \quad (15.5)$$

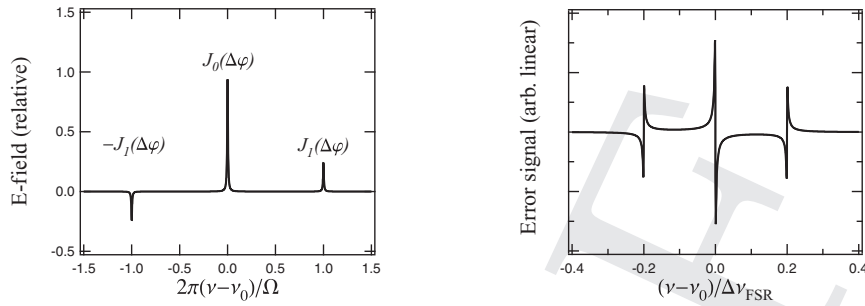
where  $L$  is the distance separating the mirrors and  $c$  is the speed of light. This condition is simply the requirement for a standing wave resonance within the cavity. Thus, the modes are spaced in frequency by  $c/2L$ , a quantity known as the free spectral range ( $\Delta\nu_{\text{FSR}}$ ). By analyzing the denominator of Equation 15.4, the width of the cavity resonance (i.e. the width of a dip in  $|\mathcal{R}|^2$ ), denoted as  $\Delta\nu_{\text{FWHM}}$ , is related to the free spectral range by

$$\mathcal{F} = \frac{\Delta\nu_{\text{FSR}}}{\Delta\nu_{\text{FWHM}}} = \frac{\pi |r|}{1 - |r|^2} = \frac{\pi \sqrt{R}}{1 - R}. \quad (15.6)$$

Here  $R \equiv |r|^2$ , and is the intensity reflection coefficient. This ratio,  $\mathcal{F}$ , is known as the cavity finesse and, as Equation 15.6 shows, depends only on the mirror properties.

### 15.2.1 Pound–Drever–Hall locking

As seen in the previous Section, an optical cavity defines a series of narrow resonances. A common way to stabilize a laser to such a resonance is through a frequency modulation locking technique. The most commonly used and successful frequency modulation technique for laser stabilization is the Pound–Drever–Hall (PDH) stabilization scheme



(a) Electric field amplitude in Fourier space in the presence of phase modulation of depth  $\Delta\varphi$ . (b) Pound-Drever-Hall error signal as a function of laser detuning from the cavity resonance.

Figure 15.4 Pound-Drever-Hall sidebands and error signal.

(Drever *et al.*, 1983), where the frequency modulation is performed at a much higher frequency than the cavity linewidth.

There are several reasons for the widespread adoption of PDH locking. First, there are no restrictions upon the phase modulation frequency, as long as it is larger than the cavity linewidth. A higher modulation frequency gives the lock immunity to common laser amplitude noise offsets and also permits the use of resonant electro-optic modulators (EOMs). Additionally, in the PDH scheme, the lock bandwidth is not restricted by the cavity linewidth, allowing extremely narrow cavity resonance features to provide high-bandwidth stabilization.

Several reviews of PDH locking and laser feedback control theory exist (Day *et al.*, 1992; Mor and Arie, 1997; Black, 2001; Bava *et al.*, 2006). Here, we briefly discuss the important results of the PDH locking technique.

In order to measure the PDH error signal from an optical cavity, the laser must first be phase modulated. A phase modulated signal can be decomposed into a carrier and sidebands using the Jacobi–Anger expansion (Hils and Hall, 1987):

$$E_0 e^{-i2\pi f_0 t - i\Delta\varphi \sin(\Omega t)} = E_0 J_0(\Delta\varphi) e^{-i2\pi f_0 t} + E_0 \sum_{n=1}^{\infty} J_n(\Delta\varphi) [e^{-i(2\pi f_0 + n\Omega)t} + (-1)^n e^{-i(2\pi f_0 - n\Omega)t}]. \quad (15.7)$$

Here, the term  $\Delta\varphi$  is the phase modulation depth and  $\Omega$  is the phase modulation frequency. From this expansion, it is clear that the first order sidebands are 180 degrees out of phase (as are all odd order sidebands), as pictured in Figure 15.4. When the phase modulation frequency is well outside the cavity bandwidth, these sidebands are sufficiently detuned from the cavity resonance such that they are promptly reflected from the cavity unaffected. The carrier, which is near the cavity resonance, is affected by the complex response of the cavity (as shown in Figure 15.3 and given in Equation 15.4) and interferes with the phase modulation sidebands upon reflection.

This interference term can be explored by assuming that the phase modulation sidebands are completely reflected and finding the time-dependent reflected optical power,  $P_{\text{ref}}(t)$ , when the carrier is near resonance. Making use of only the first order sidebands of Equation 15.7,

$$\begin{aligned} P_{\text{ref}}(t) &= \frac{1}{2} |E_{c, \text{ref}} + E_s e^{-i\Omega t} - E_s e^{i\Omega t}|^2 \\ &= P_{c, \text{ref}} + 2P_s - 2 \Im \{E_{c, \text{ref}} E_s^*\} \sin(\Omega t) + 2\Omega \text{ terms.} \end{aligned} \quad (15.8)$$

Here,  $E_{c, \text{ref}}$  ( $P_{c, \text{ref}}$ ) is the reflected electric field amplitude (power) in the carrier and  $E_s$  ( $P_s$ ) is the reflected electric field amplitude (power) in the sidebands. Keeping everything that oscillates at  $\Omega$  or below, and making use of Equations 15.7 and 15.4,

$$\begin{aligned} P_{\text{ref}}(t) &= P_0 [J_0^2(\Delta\varphi) |\mathcal{R}|^2 + 2J_1^2(\Delta\varphi)] \\ &\quad + 4P_0 J_0(\Delta\varphi) J_1(\Delta\varphi) \Im \{\mathcal{R}\} \sin(\Omega t). \end{aligned} \quad (15.9)$$

When the carrier is less than a cavity linewidth from resonance,

$$\Im \{\mathcal{R}\} \simeq \frac{-2|t|^2 \mathcal{F}}{(1 - |r|^2) \Delta\nu_{\text{FSR}}} \delta\nu. \quad (15.10)$$

Here,  $\delta\nu$  is the laser detuning from cavity resonance given by  $\delta\nu = \nu_{\text{laser}} - \nu_{\text{cavity}}$ . The term in Equation 15.9 that oscillates as  $\sin(\Omega t)$  is thus given by

$$\mathcal{D} \delta\nu \sin(\Omega t), \quad (15.11)$$

where we have used the definition

$$\mathcal{D} \equiv -\frac{8P_0 J_0(\Delta\varphi) J_1(\Delta\varphi)}{\Delta\nu_{\text{FWHM}}} \left( \frac{|t|^2}{1 - |r|^2} \right), \quad (15.12)$$

along with the relationship  $\Delta\nu_{\text{FSR}}/\mathcal{F} = \Delta\nu_{\text{FWHM}}$  to derive Equation 15.12.

Equation 15.11 gives the component of optical power that oscillates at the phase modulation frequency. For small detunings, the amplitude is linear in  $\delta\nu$ , and can thus be used to lock the laser to the optical cavity after the optical power has been detected on a photodiode and demodulated. The degree to which the amplitude changes for a given detuning is characterized by the parameter  $\mathcal{D}$ , which, as should be expected, varies inversely with cavity linewidth and is proportional to the product of the zero and first-order Bessel functions. In passing, we note that this can be used to define an optimal modulation depth, given by  $\Delta\varphi = 1.08$ . By measuring this oscillating RF signal, and demodulating by mixing in the proper quadrature at the frequency  $\Omega$ , a linear error signal can be obtained with which to feed back upon the laser frequency.

While Equation 15.11 describes the behavior of the error signal near the cavity resonance, one may go a step further and include the frequency dependence of  $\Im\{\mathcal{R}\}$  to calculate the shape of the error signal over a broader range, as shown in Figure 15.4 (Mor and Arie, 1997). When this detail is included, it can be shown that the error signal of Equation 15.11 needs to be multiplied by a single-pole low-pass filter function with a corner frequency

equal to the cavity half-width. This effect can be compensated for by appropriate servo design, such that the lock bandwidth need not be limited by the cavity linewidth. Physically, this low-passing effect represents a transition from a regime in which the cavity is sensitive to frequency fluctuations of the laser to one in which the error signal is proportional to phase fluctuations of the laser. As expected, this transition occurs at the cavity half-width.

### 15.2.2 Sources of lock error

There are two important considerations when frequency stabilizing a laser by locking it to an optical cavity. The first is that the reference cavity optical length must be as stable as possible and will be discussed in Section 15.3. However, an equally important question is whether there are any issues that can prevent a laser from precisely tracking the reference cavity resonance, due to either technical or quantum effects.

The most fundamental but least important source of error in cavity locking systems is quantum noise (see, e.g., Salomon *et al.* (1988); Day *et al.* (1992)). The optical power spectrum of shot noise on the light at the detector is given by the single-sided power spectral density

$$G_P = 2h\nu P_{\text{opt}} \quad [\text{W}^2/\text{Hz}]. \quad (15.13)$$

Thus, assuming  $|r|^2 + |t|^2 = 1$ , the expected frequency noise due to shot noise in the most ideal case (and with an ideal demodulator) is

$$G_\nu = \frac{G_P}{\eta D^2} = \frac{h\nu \Delta\nu_{\text{FWHM}}^2}{16\eta P_0 J_0^2} \quad [\text{Hz}^2/\text{Hz}], \quad (15.14)$$

where  $\eta$  takes into account the detector quantum efficiency and  $\nu = c/\lambda$  is the optical frequency. Substituting in the very modest parameters  $\lambda = 1 \mu\text{m}$ ,  $P_0 = 10 \mu\text{W}$ ,  $\eta = 0.5$ , and  $\Delta\nu_{\text{FWHM}} = 10 \text{ kHz}$ , the very low shot noise floor of  $G_\nu = 4 \times 10^{-7} \text{ Hz}^2/\text{Hz}$  can be achieved. This can be related to the locked laser linewidth by

$$\Delta\nu_{\text{locked}} = \pi G_\nu, \quad (15.15)$$

where it is assumed that  $G_\nu$  is white noise. For the parameters given above, this results in a locked linewidth of  $1 \mu\text{Hz}$ . Thus, for high-finesse cavities, the shot noise locking limit is far below any cavity locking result, even in experiments designed to exclude other technical and thermal effects (Salomon *et al.*, 1988). This indicates that in practical situations, “technical” effects are most important.

Residual amplitude modulation (RAM) is a term that collectively describes a variety of effects that induce amplitude modulation at the phase modulation frequency. For example, temperature-dependent parasitic etalons within the optical system can induce RAM which is then demodulated along with the cavity error signal. This causes an offset to be introduced in the locking system. Other effects that can cause RAM are typically related to the phase modulation device, most often an electro-optic crystal-based (e.g. LiNbO<sub>3</sub>, ADP, KDP) modulator. For instance, stress-induced birefringence in crystal devices can rotate the

principle crystal axis, creating not only an electric field-dependent phase shift, but also a corresponding polarization rotation, which can be distributed across the optical wave front.

While in many cases a temperature-controlled electro-optic (EO) crystal has low enough RAM for acceptable performance, a certain degree of success has been achieved by using a DC electric field on crystal-based EO modulators to actively servo the RAM (Wong and Hall, 1985). However, beam pointing deviations can cause slightly different regions of the crystal to be sampled, causing the phase of the RAM to shift, and limiting the effectiveness of the active system.

It is important to note that the effect of RAM on laser stability is reduced for cavities with narrower resonances due to the fact that a given fractional change in RAM results in a smaller change in frequency for a narrower resonance. Thus, for a given cavity length, higher cavity finesse is always desirable to help mitigate RAM-induced line pulling.

### 15.3 Mechanical design of optical reference cavities

Despite the considerable challenges present in building a high-quality cavity locking system that is free from residual frequency offsets, these effects are not what limit most high-finesse optical cavity frequency references. Instead, perturbations to the length of optical reference cavity are ultimately what limit the frequency stability. These perturbing effects fall into two categories: mechanical and thermal perturbations that are not fundamental, i.e. that are non-statistical in origin; and fundamental statistical fluctuations in the cavity spacer, substrate, and coatings that arise from their contact with a thermal reservoir at room (or cryogenic) temperature.

In this Section, we discuss non-statistical perturbing effects and describe methods for their mitigation. These mechanical effects can be divided into two categories: those caused by vibrations (accelerations) that structurally deform the cavity, and those that couple through the coefficient of thermal expansion (CTE) of the cavity materials. Use of finite element analysis to optimize cavity geometries and choice of materials has drastically reduced and elucidated these effects.

#### 15.3.1 *Vibration sensitivity*

Although optical cavity mirrors and spacers are typically made out of a rigid substance, such as ultra low expansion glass (ULE), the length stability requirements are extremely stringent for sub-Hz lasers. As can be seen from Equation 15.5, the fractional frequency change of a cavity resonance is directly related to the fractional length change by

$$\frac{\Delta\nu}{\nu} = -\frac{\Delta L}{L}. \quad (15.16)$$

The current world record for cavity stabilization was set in 1999 with 1 s stability at  $3 \times 10^{-16}$  and employed a very impressive vibration isolation scheme in order to keep the cavity length constant – effectively suspending the entire optical table on giant rubber

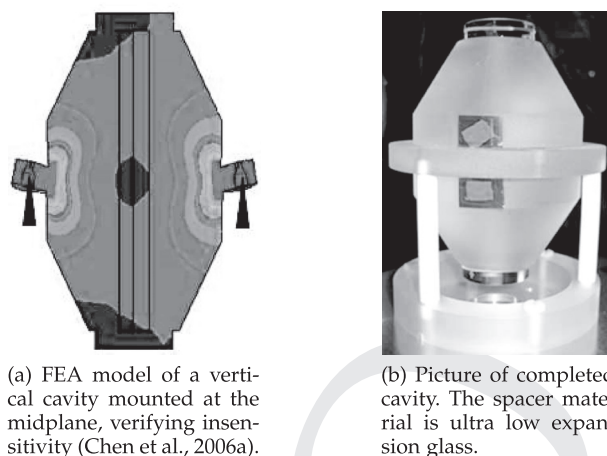


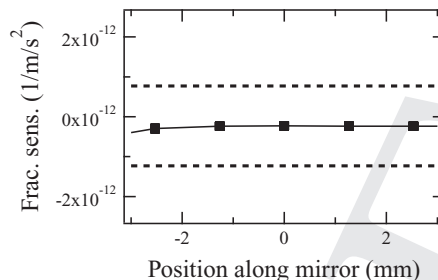
Figure 15.5 Vertical cavity mounting geometry using the symmetric supporting scheme. Finite element analysis (FEA), figure (a), can be used to fine-tune the mounting geometry.

bands (Young *et al.*, 1999). Although the cavity length we discuss is the effective length sensed by the optical field, which is averaged over the mirror surface, it is still astounding that the length stability needed for a sub-Hz laser is sub-fm ( $10^{-15}$  m) – the length scale of the proton radius! It should come as no surprise that length stability at or below one part in  $10^{15}$  takes significant engineering effort.

One approach that significantly reduces the dependence on vibration-isolating structures is to design the cavity spacer such that the mirror–spacer system is insensitive to vibrations. An intuitive way to achieve this is to mount the cavity at its midplane in the vertical direction (Notcutt *et al.*, 2005). In this way, the top and bottom mirrors move equal amounts when subject to vibrations along the vertical axis. However, one can only get so far exploiting intuitive geometry for the simple reason that the support structure breaks perfect vertical symmetry. Thus, to finalize any cavity design, finite element analysis (FEA) must be employed (Chen *et al.*, 2006a). This technique can be applied to a variety of cavity geometries and tailored to a specific design goal, such as insensitivity in a specific direction.

One system that exploits the benefits of vertical symmetry (Ludlow *et al.*, 2007), shown in Figure 15.5(b), has a measured vibrational sensitivity in the vertical direction of  $30 \text{ kHz}/(\text{m/s}^2)$  representing a fractional sensitivity of  $7 \times 10^{-11}/(\text{m/s}^2)$ . A more recent example of a stable cavity based on a vertical geometry has shown even better vibrational insensitivity by the FEA technique at the level of  $10^{-11}/(\text{m/s}^2)$  (Millo *et al.*, 2009). These results are quite good given that the highest grade commercial isolation platforms can give isolation performance at the  $50 \text{ ng}/\sqrt{\text{Hz}}$  level, resulting in a vibration-limited frequency noise performance of order  $10 \text{ mHz}/\sqrt{\text{Hz}}$  for the sensitivities exhibited by modern cavities in the visible spectrum.

In principle, one is not restrained to vertical configurations. In fact, there may be good reason to choose a horizontal configuration, especially if it is expected that the majority of



Mirror displacements per  $\text{m/s}^2$  of vertical acceleration as a function of vertical distance along the mirror surface. The support positions have been optimized to reduce length sensitivity for vertical accelerations. The dashed horizontal lines indicate the estimated uncertainty due to finite mesh size effects.

Figure 15.6 Finite element analysis (FEA) of a 40 cm cavity in development at JILA.

vibrations will be in the vertical direction. Through FEA, results comparable to and even better than those obtained with vertical mounting schemes have been obtained (Webster *et al.*, 2007; Millo *et al.*, 2009). Other motivating factors include structural stability, especially for larger cavities, and the experimental ease of access for horizontal geometries. Most importantly, in the horizontal configuration, the coupling of vertical accelerations to deviations along the optical axis is reduced by the Poisson’s ratio, representing roughly an 80% reduction in sensitivity. However, horizontal accelerations can still couple into mirror displacement, although the inherent symmetry in the two horizontal axes limits this effect. Figure 15.6 shows an FEA model of a 40 cm ULE cavity under development at JILA. Sensitivity to vertical accelerations has been eliminated in the FEA model by choice of support points.

### 15.3.2 Thermomechanical perturbations

The most common cavity spacer and mirror substrate materials for ultrastable reference cavities are ULE, fused silica (FS), sapphire, and silicon. The coefficients of thermal expansion (CTEs) of these materials are shown in Figure 15.7. Owing to large room-temperature CTEs, the latter two materials have primarily been used at cryogenic temperatures (Richard and Hamilton, 1991; Seel *et al.*, 1997; Müller *et al.*, 2003a). See Chapter 8 for more on cryogenics.

In general, a cavity made of a uniform-CTE material will experience a fractional length change given by

$$\Delta L/L = \alpha(T)\delta T + \frac{1}{2}\alpha'(T)\delta T^2 + \mathcal{O}(\delta T^3), \quad (15.17)$$

where  $\alpha(T)$  is the CTE at the operating temperature,  $T$ ,  $\alpha'(T)$  is its first derivative, and  $\delta T$  are small temperature variations. Ideally, one operates a reference cavity around a

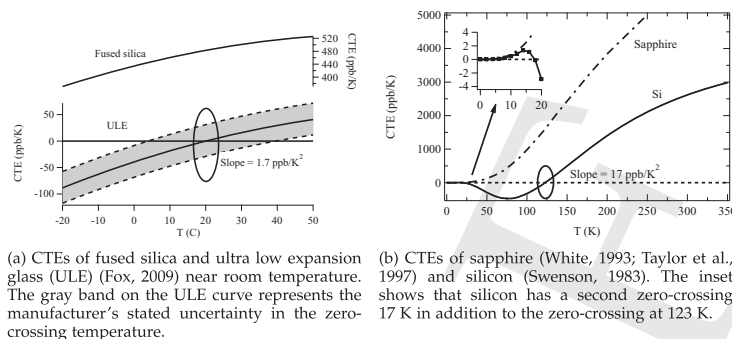


Figure 15.7 Temperature dependence of coefficients of thermal expansion (CTEs) of common cavity spacer and substrate materials. See also Section 7.3.

zero-crossing temperature of a material's CTE,  $T_0$ , defined as

$$\alpha(T_0) = 0. \quad (15.18)$$

In the case of sapphire, which has no zero crossing, optimal operation is at cryogenic temperatures which reduce the CTE to an acceptable level. Taking Equation 15.17 in the vicinity of a zero crossing and substituting in  $\alpha'(T_0) = 1.7 \times 10^{-9}/K^2$  for ULE, it can be seen that the temperature needs to be stable below 1 mK for relative length stability at the  $10^{-16}$  level. While this is in principle quite difficult, the large thermal mass of the ULE spacer tends to limit temperature effects to longer time scales. Mechanical coupling from the vacuum chamber itself, not the CTE of the spacer material, can introduce the biggest temperature-dependent frequency shift. Thus, care should also be taken to mechanically decouple the cavity support structure from the chamber. As seen in Figure 15.5(b), this can be accomplished with a separate ULE piece (in this case a ring).

In the case of a cavity with a mirror substrate made out of a different material than the spacer, extra complications arise. The two materials are typically optically contacted very firmly, such that the mismatch of CTEs causes an auxiliary mechanical effect, effectively causing the mirror substrate to bend. This modifies the effective CTE,  $\alpha_{\text{net}}$ , such that (Notcutt *et al.*, 1995)

$$\alpha_{\text{net}} = \alpha_{\text{spacer}} + 2\delta \frac{R}{L} (\alpha_{\text{mirror}} - \alpha_{\text{spacer}}) + \Gamma. \quad (15.19)$$

Here,  $R$  is the mirror radius and  $L$  is the cavity length. The term  $\delta$  describes thermo-mechanical stresses coupling into length change and  $\Gamma$  accounts for deviations from the ideal model (Fox, 2009). Thermo-mechanical finite element analysis can be used to find  $\delta$  for a given cavity geometry, such that  $\alpha_{\text{net}}$  can be found and minimized by operating at the new zero-crossing temperature (Fox, 2009; Legero *et al.*, 2010).

Finally, it is worth noting that there has been good success tuning the zero cross point by contacting an additional piece of ring-shaped ULE glass to the back of the mirror substrate, effectively “sandwiching” the substrate between two equivalent CTE materials. By varying

the parameters of the ring-shaped piece of glass, one can engineer a more favorable  $T_0$  (Legero *et al.*, 2010).

## 15.4 Statistical thermal noise

The second class of thermally-driven length fluctuations in optical cavities are more fundamental in origin. These fluctuations have been discussed in Chapters 1, 3, 4, 7, and 9. Here we apply the developed formalism to the case of optical cavities.

### 15.4.1 Brownian motion

The first, and typically most important, type of thermal noise for precision optical measurements is the Brownian motion of the constituents of the optical system. In the case of a cavity, the components of concern are the spacer, mirror substrate, and mirror coatings. At temperature  $T$ , after appropriately weighting the displacement by the beam profile (see Chapter 1), the one-sided power spectral density of position fluctuations (in units of  $\text{m}^2/\text{Hz}$ ) for each of these components at Fourier frequency  $f$  are (Harry *et al.*, 2002; Numata *et al.*, 2004)

$$G_x^{\text{substrate}}(f) = \frac{2k_B T}{\sqrt{\pi^3} f} \frac{1 - \sigma^2}{w_m Y_s} \phi_s, \quad (15.20)$$

$$G_x^{\text{coating}}(f) = \frac{2k_B T}{\sqrt{\pi^3} f} \frac{1 - \sigma^2}{w_m Y_s} \left\{ \frac{1}{\sqrt{\pi}} \frac{d}{w_m Y_s Y_c (1 - \sigma_c^2) (1 - \sigma_s^2)} \right. \\ \left. \times [Y_c^2 (1 + \sigma_s)^2 (1 - 2\sigma_s)^2 \phi_{\parallel} + Y_s Y_c \sigma_c (1 + \sigma_s) (1 + \sigma_c) (\phi_{\parallel} - \phi_{\perp}) \right. \\ \left. + Y_s^2 (1 + \sigma_c)^2 (1 - 2\sigma_c) \phi_{\perp} \right\}, \quad (15.21)$$

$$G_x^{\text{spacer}} = \frac{2k_B T}{f} \frac{L}{3\pi^2 R_{\text{spacer}}^2} \frac{\phi_{\text{spacer}}}{Y_{\text{spacer}}}. \quad (15.22)$$

The parameters are the same as defined previously in Chapters 4 and 7, and are presented again in Table 15.1 for completeness.

Two qualitative remarks can be made at this point. First, both the substrate and coating displacement noise power spectral densities, given by Equations 15.20 and 15.21, respectively, do not depend on the length of the cavity. This is due to the fact that the fluctuations are localized to the mirror surface and this property can be exploited in order to reduce frequency noise. By increasing the cavity length, the fractional length fluctuations decrease, resulting in a substrate and coating thermal noise-induced frequency noise spectral density that is proportional to  $1/L^2$ . Secondly, while the spacer thermal noise contribution scales with length, and inversely with spacer radius,  $R_{\text{spacer}}$ , its contribution to the total fractional length change of the cavity in fact decreases with length. This is due to the conversion from power spectral densities to fractional frequency fluctuations involving division by

Table 15.1 Summary of the parameters used in the text.

Definition of parameters	
$w_m$	Beam $1/e^2$ intensity radius
$d$	Coating thickness
$\phi_s$	Substrate loss angle
$\phi_{\perp(\parallel)}$	Coating loss angle perpendicular (parallel) to substrate
$Y_{s(c)}$	Substrate (coating) Young's modulus
$\sigma_{s(c)}$	Substrate (coating) Poisson's ratio
$\alpha_{s(c)}$	Substrate (coating) coefficient of thermal expansion
$\kappa_{s(c)}$	Substrate (coating) thermal conductivity
$C_{s(c)}$	Substrate (coating) heat capacity
$f_c^{\text{sub(coat)}}$	Substrate (coating) cutoff frequency

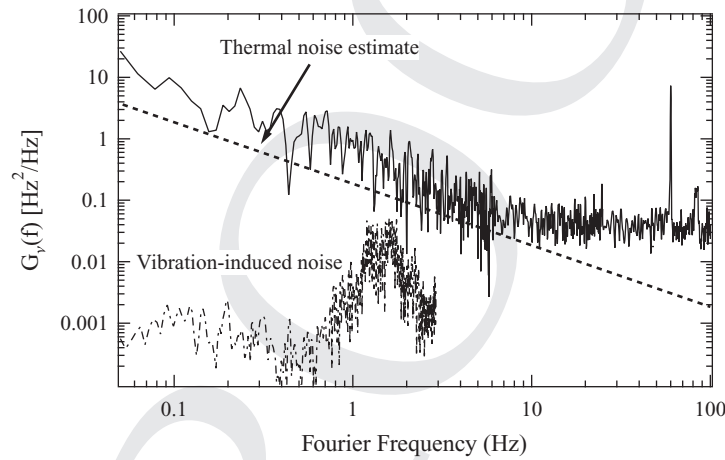


Figure 15.8 Measured frequency noise of the cavity shown in Figure 15.5. The noise frequency spectrum is thermal noise limited to 10 Hz, where the photon shot noise and detector electronic noise begin to dominate.

$L^2$ . Additionally, longer optical cavities typically have larger radii in order to maintain favorable mounting geometry, meaning that as  $L$  increases, so too does  $R_{\text{spacer}}$ .

Current experiments are at or near the expected thermal noise limitations set by the substrate and coating Brownian thermal noise alone. This is because the spacer contribution of Equation 15.22 is generally an order of magnitude below mirror thermal noise for typical cavity aspect ratios. Figure 15.8 shows an example of an experimentally obtained frequency spectrum taken from a comparison between two ultra-stable lasers (of the type shown in Figure 15.5), which approximately agrees with the Brownian thermal noise limit (Ludlow *et al.*, 2007). See also Chapter 5 for direct observations of coating thermal noise in optical

cavities. Also shown in Figure 15.8 is the vibration-limited frequency noise spectrum, which is well below the thermal noise floor, indicating that vibration noise does not contribute to the observed spectrum.

One clear avenue to decrease this noise limit is to decrease the material losses (see Chapter 4), lower the temperature (see Chapter 8), or do both. However, the situation is not so simple. For example, the loss angle of fused silica begins to increase sharply at temperatures below  $\sim 250$  K, ultimately suffering an almost four orders of magnitude increase before it levels off at 50 K, completely eliminating the benefit of operating at these temperatures (Braginsky *et al.*, 1985; Schnabel *et al.*, 2010). However, crystalline materials such as sapphire (Braginsky *et al.*, 1985; Uchiyama *et al.*, 1999), calcium fluoride (Nawrodt *et al.*, 2007a), and silicon (McGuigan *et al.*, 1978; Rowan *et al.*, 2003; Schnabel *et al.*, 2010) offer the benefits of low thermal expansion and low loss angle at cryogenic temperatures. Unfortunately, typical coating loss angles exhibit an approximate factor of 3 increase at cryogenic temperatures (see Chapters 4 and 8), which offsets some of the gains of operating at low temperatures. We note in passing that there is an active search for low-loss coating materials or dopants to reduce the mechanical loss of the existing coating materials (Harry *et al.*, 2006a). It also becomes increasingly difficult to shield cryostat vibrations at very low temperatures, due to the large cooling powers required. Chapter 8 contains a more complete discussion of the advantages and disadvantages of cryogenics for thermal noise.

A powerful alternative approach to reduce Brownian coating and substrate thermal noise relies not on reducing the temperature, but instead on using specially shaped beams, such as Mesa, conical, or higher order Laguerre–Gauss beams (Bondaescu *et al.*, 2008). This has the effect of better averaging the position fluctuations of the mirror surface due to thermal noise. While one could simply envision working near the stability edge of an optical cavity with typical spherical mirrors to create larger mode-areas on the mirrors, the input pointing stability requirements become more stringent in these regimes. Specially shaped beams have their own challenges, however, especially controlling the manufacturing process to create satisfactory mirror profiles in the small-scale optics used in optical cavities (Tarallo *et al.*, 2007) (see also Section 2.7). See Chapter 13 for a detailed discussion of beam shaping for thermal noise reduction.

#### **15.4.2 Thermo-optic noise**

Substrate thermoelastic and coating thermo-optic noise have been studied as a noise source for gravitational wave detectors (Cerdonio *et al.*, 2001; Braginsky and Vyatchanin, 2003a; Evans *et al.*, 2008) where it potentially has important sensitivity implications. Substrate thermoelastic noise is discussed in Chapter 7, coating thermo-optic noise is covered in Chapter 9, and gravitational wave detectors in general are the topic of Chapter 14. In contrast to Brownian motion of the mirror substrate and coatings, thermo-optic noise arises from fundamental temperature fluctuations in the bulk material coupling to the coefficient

of thermal expansion. These temperature fluctuations can be described by the well-known expression (Braginsky *et al.*, 1999)

$$\langle \delta T^2 \rangle = \frac{k_B T^2}{\rho C V}. \quad (15.23)$$

Here  $\rho$  is the material density,  $C$  is the heat capacity per unit mass, and  $V$  is the volume over which the temperature fluctuations are considered.

There are two Fourier frequency regimes in the analysis of thermo-optic noise. The first is where the thermal diffusion length scale is smaller than the laser spot size, allowing an averaging effect to take place. This regime is known as the adiabatic limit and only applies to time-domain Fourier frequencies  $f$  that satisfy  $f \gg f_c$  where the cutoff frequency,  $f_c$ , is given by

$$f_c = \frac{\kappa}{\pi w_m^2 \rho C}. \quad (15.24)$$

Owing to the small beam sizes ( $\sim 100 \mu\text{m}$ ) and interest in the frequency noise spectrum all the way to DC in cavity-stabilized laser systems, one must be aware that  $f_c$  is typically in the 1 Hz range. Thus, consideration of thermo-optic noise in the second regime, at Fourier frequencies  $f < f_c$ , is necessary for a complete picture of the various contributions to the frequency noise of cavity stabilized lasers. See also Section 8.2.5.

#### *Substrate thermoelastic noise*

To date, many optical cavities have employed mirrors made from ULE substrates (Ludlow *et al.*, 2007; Alnis *et al.*, 2008b). As a result, consideration of substrate thermoelastic noise is not necessary for these systems, as the material CTE is close to zero. (see Chapter 7 for the relationship between CTE and thermoelastic noise.) This approximation has also been made in the case of fused silica substrates (Numata *et al.*, 2004). In fact, while alarming predictions for substrate thermoelastic noise can be obtained by extrapolating the high-frequency behavior of fused silica to DC, using the appropriate expression for the low-frequency behavior verifies that the substrate thermoelastic noise is at least an order of magnitude below the Brownian noise of the substrates and coatings.

It has been shown (Braginsky *et al.*, 1999; Cerdonio *et al.*, 2001) that the one-sided power spectral density of mirror length fluctuations due to the substrate is

$$G_x^{\text{TE,sub}}(f) = \frac{4}{\sqrt{\pi}} \alpha_s^2 (1 + \sigma_s)^2 \frac{k_B T^2 w_m}{\kappa_s} J[\Omega(f)]. \quad (15.25)$$

(see Chapter 7 for a full discussion of substrate thermoelastic noise.) Here,  $\Omega(f) = f/f_c^{\text{sub}}$ , and  $J[\Omega]$  is given by

$$J[\Omega] = \sqrt{\frac{2}{\pi^3}} \int_0^\infty du \int_{-\infty}^\infty dv \frac{u^3 e^{-u^2/2}}{(u^2 + v^2) [(u^2 + v^2)^2 + \Omega^3]}. \quad (15.26)$$

While the integral can be evaluated numerically, it is more instructive to calculate thermal noise in the low and high frequency limits. Specifically<sup>1</sup>,

$$G_x^{\text{TE,sub}} \rightarrow \frac{8\sqrt{2}}{3\pi} \alpha_s^2 (1 + \sigma_s)^2 \frac{k_B T^2}{\sqrt{2\pi f \kappa_s \rho_s C_s}}, \quad \Omega \ll 1 \quad (15.27)$$

$$G_x^{\text{TE,sub}} \rightarrow \frac{16}{\sqrt{\pi}} \alpha_s^2 (1 + \sigma_s)^2 \frac{k_B T^2 \kappa_s}{(2\pi f \rho_s C_s)^2 w_m^3}, \quad \Omega \gg 1. \quad (15.28)$$

These Equations indicate that at low frequencies, thermoelastic noise rises less rapidly than extrapolated from the high-frequency behavior. Qualitatively, this effect can be explained as a crossover from the regime where the thermal diffusion length is smaller than the spot size to one where it is larger. Thus, this change in behavior can be thought of as an averaging effect that is no longer valid at low frequencies (Cerdonio *et al.*, 2001; Braginsky and Vyatchanin, 2003a).

#### *Coating thermo-optic noise*

A second way that optical cavities are sensitive to thermodynamic temperature fluctuations are through a pair of correlated mechanisms present in the mirror coatings: thermorefractive and thermoelastic effects, collectively called thermo-optic noise. Thermo-optic noise is discussed in detail in Chapter 9. It has been shown that the typically opposite signs of these coherent mechanisms reduces their impact (Evans *et al.*, 2008) and the total effect can be written as

$$G_x^{\text{TO}}(f) = G_{\Delta T}(f) \left( \bar{\alpha}_c - \bar{\beta}_c - \bar{\alpha}_s \frac{C_c}{C_s} \right)^2. \quad (15.29)$$

The term in parentheses is the coherent sum of thermoelastic and thermorefractive effects; the thermo-optic noise. The parameter  $\bar{\alpha}_c$  ( $\bar{\alpha}_s$ ) is the effective coating (substrate) coefficient of thermal expansion, and  $\bar{\beta}_c$  is the effective coating thermorefractive coefficient. The term  $G_{\Delta T}(f)$  is the power spectral density of temperature fluctuations given by

$$G_{\Delta T}(f) \rightarrow \frac{2k_B T^2}{\pi w_m^2 \sqrt{\pi f \kappa_c \rho_c C_c}}, \quad \Omega \gg 1. \quad (15.30)$$

#### **15.4.3 Total thermal noise contribution to cavity frequency stability**

The total thermal noise is given by

$$G_x^{\text{tot}} = \sum_{L,R} G_x^{\text{TO}} + \sum_{L,R} G_x^{\text{TE}} + \sum_{L,R} G_x^{\text{substrate}} + \sum_{L,R} G_x^{\text{coating}} + 2G_x^{\text{spacer}}, \quad (15.31)$$

where the sum over left and right (L, R) takes into account that the beam waist is potentially different at the left and right mirrors. The factor of two in front of  $G_x^{\text{spacer}}$  is because this term is always equivalent at each mirror.

<sup>1</sup> Equation 15.27 differs from Equation 8.4 in the numerical prefactor, but only by less than 10%. The reason for this discrepancy is under investigation, but the numerical difference should not be significant in most applications.

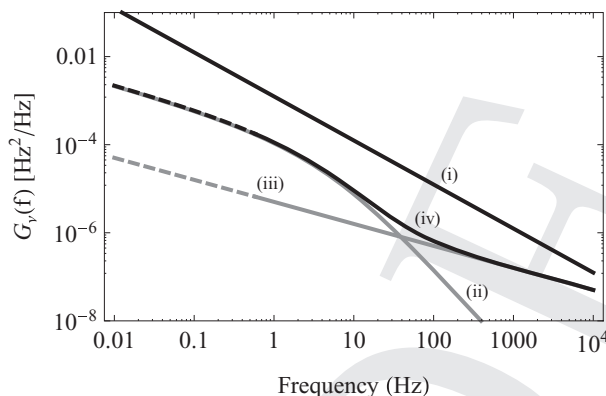


Figure 15.9 Thermal noise for a 40 cm-long (approximate radius 7 cm) cavity at 698 nm with fused silica mirror substrates and 1 m radius of curvature/planar mirror geometry (see also Figure 15.6). The temperature is 300 K. (i) Sum of mirror substrate and coating, and cavity spacer Brownian noise. (ii) Substrate thermoelastic noise. (iii) Coating thermo-optic noise. (iv) Sum of coating thermo-optic and substrate thermoelastic noise contributions. The dotted regions indicate frequency regimes where  $f \leq f_c$  (i.e. frequencies below the adiabatic limit).

Converting the total length fluctuation power spectral density,  $G_x^{\text{tot}}$ , into optical frequency deviations can be accomplished by use of Equation 15.16, which directly relates fractional length change to frequency fluctuations. We obtain

$$G_v^{\text{tot}} = \nu_0^2 G_x^{\text{tot}} / L^2, \quad (15.32)$$

where  $L$  is the length of the cavity and  $\nu_0$  is the laser's optical frequency. Current state of the art systems have a thermal noise floor that is approximately an order of magnitude above the vibration-limited noise floor (Ludlow *et al.*, 2007). The results of Equation 15.32 are shown in Figure 15.9, detailing the different contributions of the thermal noise for the specific case of the 40 cm-long JILA ULE cavity with FS mirrors investigated in Figure 15.6.

### 15.5 Atomic clock applications of frequency-stabilized lasers

A confluence of two key technologies – femtosecond laser frequency combs and ultrastable lasers – has enabled a new class of atomic clocks based not upon microwave frequency transitions but instead upon extremely narrow optical transitions in neutral atoms and ions. This revolution in precision science continues to progress as the physics behind minute effects continues to be unraveled and quantum technologies are increasingly being employed to gain signal size and robustness, further increasing clock accuracy. Additionally, neutral atom clocks stand to gain an order of magnitude in stability with the advent of next-generation ultrastable laser systems with lower thermal noise.

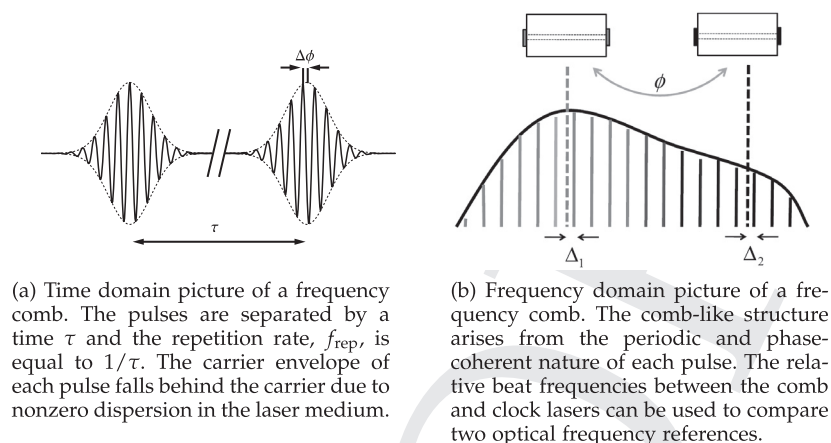


Figure 15.10 Time and frequency representations of a frequency comb.

### 15.5.1 Frequency combs

No discussion of ultrastable lasers and atomic clocks would be complete without introducing optical frequency combs. Femtosecond laser-based optical frequency combs have revolutionized the field of optical frequency metrology (Udem *et al.*, 2002; Cundiff and Ye, 2003). With laser media ranging from bulk Ti:Sapphire and optical fibers to microtoroidal resonators, the frequency comb revolution shows no signs of slowing down. The spectral coverage of frequency combs has been demonstrated to span the mid-IR to the vacuum ultraviolet (Gohle *et al.*, 2005; Yost *et al.*, 2009; Adler *et al.*, 2010).

At the heart of a comb's utility is the equation that describes the optical frequency of a given mode,  $\nu_n$ , as

$$\nu_n = n f_{\text{rep}} + f_0. \quad (15.33)$$

Here,  $f_{\text{rep}} = 1/\tau$  is the comb pulse repetition rate, where  $\tau$  is the time between successive pulses. The carrier envelope offset frequency,  $f_0$ , arises from the group and phase velocities inside the laser cavity being different. It is related to the pulse to pulse carrier envelope phase slippage ( $\Delta\phi$  in Figure 15.10(a)) by

$$f_0 = \Delta\phi f_{\text{rep}} / (2\pi). \quad (15.34)$$

In principle,  $f_{\text{rep}}$  and  $f_0$  are the comb's only degrees of freedom when describing the frequency of a given "tooth" in the frequency domain.

By locking a frequency comb to an optical source and stabilizing  $f_0$  by the self-referencing technique (Jones *et al.*, 2000; Cundiff and Ye, 2003), the comb degrees of freedom are completely constrained and directly related to the optical phase of the reference laser. By making a heterodyne beat with a second laser, the phase of the two optical sources can be directly compared (Figure 15.10(b)), often across  $> 100$  THz of spectral bandwidth (Foreman *et al.*, 2007). This technique can be used to compare optical

atomic clocks based upon different atomic species to constrain the drift of fundamental constants (Rosenband *et al.*, 2008), and also allows optical frequencies to be measured against primary frequency standards with sub-Hz accuracy (Oskay *et al.*, 2006; Campbell *et al.*, 2008; Lemke *et al.*, 2009).

### 15.5.2 Precision spectroscopy and optical standards

Optical atomic clocks have now reached unprecedented levels of stability and accuracy. At the forefront of accuracy, a clock located at the National Institute of Standards and Technology (NIST), based on a single aluminum ion and probed via quantum logic spectroscopy, now has a fractional frequency uncertainty of  $8.6 \times 10^{-18}$  (Chou *et al.*, 2010). A second clock based on a mercury ion, also at NIST, is at the  $2 \times 10^{-17}$  fractional frequency uncertainty level (Rosenband *et al.*, 2008). These remarkable advances in ion-based clocks are followed closely by a new class of optical clocks based on lattice-trapped ensembles of ultracold neutral atoms, with the most accurate at the level of  $10^{-16}$  fractional uncertainty (Ludlow *et al.*, 2008; Lemke *et al.*, 2009).

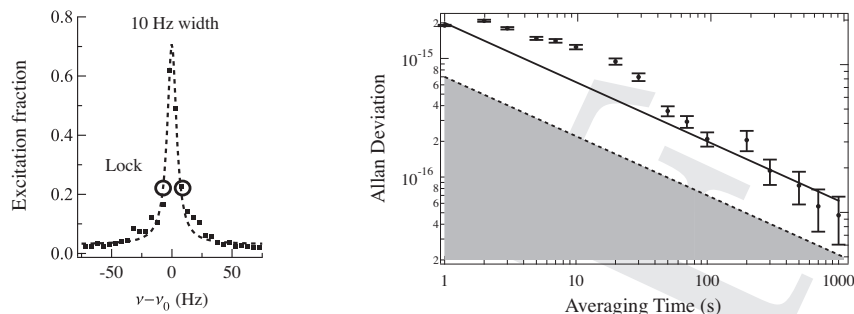
Ions and atoms make good frequency references because they are quantum systems whose transition frequencies depend very directly on the fundamental laws of physics. An atom or ion that is considered a good candidate for a clock also exhibits strong immunity to external perturbations, such as magnetic fields. Additionally, atoms or ions serving as optical standards are typically trapped sufficiently tightly that problems such as Doppler broadening and recoil shifts can be mitigated by the tight trap. These traps consist of RF Paul traps for ions (Jefferts *et al.*, 1995) and magic-wavelength optical lattices for neutral atom optical clocks (Katori *et al.*, 2003; Ye *et al.*, 2008). In addition to these general considerations, the transition used for the clock must be sufficiently narrow to provide a useful correction signal. This last condition is met by using multiply forbidden transitions in the clock atoms or ions, resulting in extremely long excited state lifetimes (in some cases  $>100$  s) and correspondingly very narrow resonance linewidths.

Atomic clocks of all types (microwave, optical trapped ion, and optical neutral atom) all rely on the same principle of operation. An oscillator with good short-term stability, the local oscillator, is used to interrogate a transition in the ion or atomic ensemble as shown in Figure 15.11(a). The local oscillator very precisely probes the energy difference of a given transition,  $\Delta E$ . The difference in energy are related to optical frequency by the well known formula

$$\Delta E = h\nu, \tag{15.35}$$

with the frequency  $\nu$  being the useful clock signal. Since  $\nu$  is an optical frequency, a frequency comb is needed if phase-coherent dissemination of a useful microwave signal is desired.

While the accuracy of single ion-based clocks is extraordinary, there is a compelling reason to pursue in parallel standards based upon ensembles of atoms: signal-to-noise.



(a) 10 Hz wide spectroscopic feature of  $^{87}\text{Sr}$  atoms as used to feedback upon the clock laser. The line has been artificially broadened for more robust operation, necessitated due to laser drift.

(b) Allan deviation of a comparison between Sr and Yb neutral atom optical standards. The dotted line indicates the quantum projection noise (QPN)-limited stability of the current system, while the shaded region shows the region of QPN accessible by use of a narrower resonance, and by increasing atom number.

Figure 15.11 Spectroscopic feature used to discipline the local oscillator laser to Sr (a) and Allan deviation of two neutral atom clocks (b).

Roughly speaking, making  $N$  parallel measurements versus one single measurement should yield a  $\sqrt{N}$  enhancement of the signal-to-noise ratio (SNR). This enhancement of the SNR for ensembles of atoms is known as quantum projection noise (Itano *et al.*, 1993). The quantum projection noise-limited stability of an optical atomic clock based on a quantity,  $N$ , of quantum references (neutral atoms or ions) is given by (Lemondé *et al.*, 2001; Sterr *et al.*, 2009)

$$\sigma(\tau) = \frac{\chi}{Q\sqrt{N}} \sqrt{\frac{T_c}{\tau}}. \quad (15.36)$$

Here,  $\chi$  is a constant of order unity that accounts for the details of spectroscopy and fraction of atoms excited,  $T_c$  is the clock operation cycle time, and  $Q$  is the fractional line quality factor, which for optical standards can be  $>10^{14}$ . Current neutral atom systems have a quantum projection noise-limited frequency stability at the sub  $10^{-15}/\sqrt{\tau}$  level (Ludlow *et al.*, 2008), and near term advances in both spectroscopic resolution and atom number make reducing this effect to below  $10^{-17}/\sqrt{\tau}$  a realistic possibility (Lodewyck *et al.*, 2009).

One roadblock to benefiting from the SNR afforded by thousands of atoms is broadband laser noise, which ends up contaminating the error signal through the Dick effect. The Dick effect is a process through which a periodic clock interrogation with spectroscopic dead time writes noise onto the correction signal, degrading long term stability (Santarelli *et al.*, 1998; Quessada *et al.*, 2003). For example, for every 1 s of time per cycle a neutral atom system might spend cooling and trapping atoms in an optical lattice, only 100 ms might be time during which spectroscopy is being performed. Thus, there is an inevitable dead time between spectroscopy sequences, resulting in a periodic sampling of the laser phase noise, and leading to aliasing of higher-frequency laser noise, deteriorating the stability.

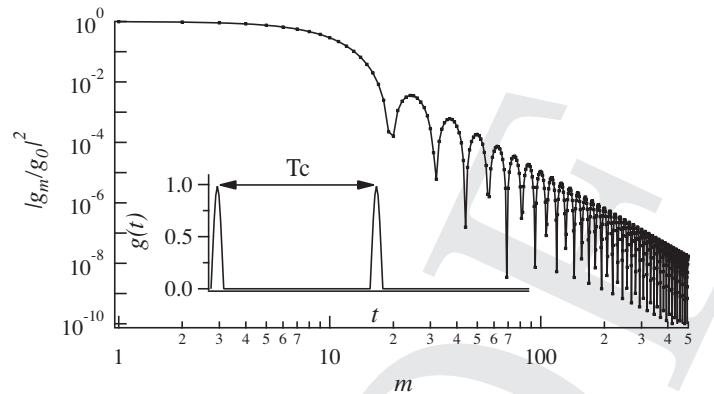


Figure 15.12 Fourier and time-domain (inset) representation of the Dick sensitivity function. With low duty-cycle clock operation, the sensitivity function covers the entire spectral region over which the clock laser is thermal noise-limited.

Specifically, it can be shown that the Dick effect-limited Allan deviation due to the aliasing mechanism is given by (Audoin *et al.*, 1998)

$$\sigma^2(\tau) = \frac{1}{\tau} \sum_{m=1}^{\infty} \frac{|g_m|^2}{g_0^2} \frac{G_v(m/T_c)}{v_0^2}. \quad (15.37)$$

Here,  $g_m$  and  $g_0$  are given by

$$g_m = \frac{1}{T_c} \int_0^{T_c} g(t) e^{i2\pi mt/T_c} dt, \quad g_0 = \frac{1}{T_c} \int_0^{T_c} g(t) dt \quad (15.38)$$

and  $G_v(f)$  is the laser frequency noise power spectral density. The function  $g(t)$  describes the spectroscopic sensitivity to a phase shift in the local oscillator laser. It is zero during the dead time, during which no spectroscopy takes place, and the details of its shape during spectroscopy are beyond the scope of this chapter. However, the important point is that the smaller fraction of the total experimental cycle the spectroscopic probe occupies, the more harmonics extend into Fourier  $m$ -space as  $g(t)$  becomes more “comb-like”. A typical sensitivity function for an optical clock with >90% dead time is shown in the inset to Figure 15.12. The normalized harmonic content of  $g(t)$ ,  $|g_m/g_0|^2$ , is shown in Figure 15.12, and only begins to roll off after the 10th harmonic in this specific case. Comparing this result to Figure 15.8, we see that for the experimentally accurate cycle time of 1 s, and the corresponding Fourier frequency range of 1–10 Hz, the most heavily weighted values of  $G_v(m/T_c)$  are squarely in the thermal noise-dominated portion of the frequency noise spectrum.

Thus, the stability of current state-of-the-art neutral atom clocks is directly tied to the thermal noise present in ultrastable cavity mirror coatings and substrates. Advances in ultrastable laser technology will permit narrower atomic resonance features to be obtained due to longer laser coherence time, while reducing fractional dead time. This represents a

triple-sided attack on the effects that currently limit neutral atom clocks: longer coherence times allow longer probe times, which increase spectroscopic line  $Q$  linearly with probe time, lowering the quantum projection noise limit; decreasing fractional dead time decreases the harmonic content of  $g_m$ , sampling less of the thermal noise spectrum; and the thermal noise level itself is lowered, making it less of a contributing factor. While reducing the experimental dead time alone is also a critical and very promising step (Lodewyck *et al.*, 2009), reducing the thermal noise-induced laser frequency noise will have immediate impact on neutral atom clocks via these three mechanisms.

## 15.6 Conclusion

Precision laser locking via optical cavities is a valuable scientific tool. With this technique, extraordinary fractional frequency stabilities as low as  $3 \times 10^{-16}$  have been reached (Young *et al.*, 1999), limited by fundamental mirror substrate and coating thermal noise. Thus, cavity-stabilized laser systems are a key enabling technology for optical frequency standards and precision measurement.

While there is no clear path to easily reducing thermal noise without making other sacrifices (e.g. larger cavities or cryogenic systems), the thermal noise-limited performance of ultrastable lasers seemingly has room for one or two more orders of magnitude improvement before the limitations of laboratory-scale technology are reached. However, state-of-the-art optical clocks based on neutral atoms are poised to benefit from even modest reductions in thermal noise, allowing quantum-limited operation to be realized.

Furthermore, exploration of effects that can degrade clock accuracy, such as density-dependent shifts (Campbell *et al.*, 2009), can be realized with the short term stability of lasers alone. By making a series of differential measurements, many residual effects that limit clock accuracy can be better understood, leading in turn to better clock accuracy.

Thus, as we look towards the next generation of optical references, we can expect advances in atomic clock technology to go hand in hand. While neutral atom clocks have the largest stake in the future of stable lasers, all frequency references in the optical domain stand to benefit from better lasers. As accuracy and precision continue to increase, so too does our ability to test fundamental physical principles.